



MOX-Report No. 35/2016

**An unfitted formulation for the interaction of an  
incompressible fluid with a thick structure via an  
XFEM/DG approach**

Zonca, S.; Formaggia, L.; Vergara, C.

MOX, Dipartimento di Matematica  
Politecnico di Milano, Via Bonardi 9 - 20133 Milano (Italy)

[mox-dmat@polimi.it](mailto:mox-dmat@polimi.it)

<http://mox.polimi.it>

# An unfitted formulation for the interaction of an incompressible fluid with a thick structure via an XFEM/DG approach

Stefano Zonca<sup>#</sup>      Luca Formaggia<sup>#</sup>      Christian Vergara<sup>#</sup>

October 6, 2016

<sup>#</sup> MOX– Modellistica e Calcolo Scientifico  
Dipartimento di Matematica  
Politecnico di Milano  
via Bonardi 9, 20133 Milano, Italy  
`stefano.zonca@polimi.it`  
`luca.formaggia@polimi.it`  
`christian.vergara@polimi.it`

**Keywords:** Unfitted meshes, Extended finite element method, Discontinuous Galerkin, Fluid-structure interaction

**AMS Subject Classification:** 65M60 , 74F10 , 65M85

## Abstract

A numerical procedure that combines an Extended Finite Element (XFEM) formulation and a Discontinuous Galerkin technique is presented, with the final aim of providing an effective tool for the simulation of three-dimensional fluid-structure interaction problems where the structure undergoes large displacements. In this work we consider thick structures immersed in a fluid domain and we focus on the description of the numerical models and on the techniques used to deal with the issues related to the implementation of XFEM in this context. Numerical results are provided to show the effectiveness of the approach.

## 1 Introduction

The study of the mechanics of the heart valves and their interaction with blood is very important for understanding their functional behaviour, for developing prosthetic valves and for post-surgery feedbacks, see, e.g, [36, 21]. In this context,

the leaflets of the aortic valve, which is at the interface between the left ventricle and the aorta, play a key role since they have a major influence on the blood fluid-dynamics in the proximity of the valve and along the aortic arch [22, 31, 37, 11]. The numerical simulation of such a scenario could provide important quantitative information about the fluid-structure interaction (FSI) arising between blood and leaflets. Unlike the vascular case, here the FSI problem requires to deal with some issues, namely the large displacements involving the leaflets, their small thickness, and the treatment of the contact.

A classical approach to deal with the *vascular* FSI problem relies on the generation of a single mesh with a fitted interface between fluid and vessel wall. While for the structure problem a Lagrangian formulation is usually considered, for the fluid one an Arbitrary Lagrangian Eulerian (ALE) approach is employed to take care about the movement of the interface and the resulting deformation of the fluid mesh induced by the displacement of the structure [13]. However, in the *valve* FSI problem this strategy may lead to a very distorted fluid mesh and in some cases a remeshing procedure may be necessary [20]. A different approach consists in considering *unfitted* meshes, where the fluid mesh is fixed on the background while the structure one is free to move independently. Within these methods, the Immersed Boundary (IB) and the Fictitious Domain (FD) methods, see, e.g., [27, 3, 18, 16, 24], are two effective techniques that were successfully employed in the case of thin valve leaflets, see, e.g., [34, 10, 2, 5, 17]. A more recent methodology is based on an unfitted formulation that allows to treat non-conforming, overlapping/unfitted meshes by writing the weak formulation of fluid and structure problems in their physical domains. This possibly leads to mesh elements with complex shape, allowing to maintain the accuracy of the standard finite element method, see, e.g. [1, 8, 23].

In this work, we consider the case of a three-dimensional (3D) structure immersed in a fluid where the solid mesh overlaps the fluid one and the interface is fitted only to the solid mesh. Due to the thin thickness of the 3D structure, which may be smaller than the characteristic fluid mesh size, the solid may split a fluid element into two subparts, thus generating two fluid polyhedra with the solid in between (in what follows we refer to this kind of elements as *split tetrahedra*). To manage this situation, we propose to use an eXtended Finite Element Method (XFEM) [19, 1], where the degrees of freedom (*dofs*) of the split elements are doubled, allowing to represent a discontinuity within the element accurately. We notice that in the literature, other, more general, definitions of XFEM have been provided [15]. Here we will refer to XFEM only when the doubling of the interface *dofs* is considered.

To glue the solution at the physical interface, we employ a Discontinuous Galerkin (DG) technique. The use of an unfitted formulation in combination with the XFEM and the DG techniques has been reported in [1] for the case of a membrane structure. In [28], the authors employ a similar formulation in 3D for the incompressible Navier-Stokes equations solely. At the best of our knowledge, this strategy is here employed for the first time for a FSI problem with thick

structure. In this work we focus on the methodological and implementational aspects. To this aim, we limit our study to small deformations of the structure domain.

The paper is organized as follows. In Section 2 we present the fluid-structure interaction problem and the corresponding XFEM/DG discretization. In Section 3 we describe how to solve the major technical issues encountered by the proposed method. In Section 4 we show several 3D numerical tests to assess and validate the proposed method. Finally, Section 5 is devoted to conclusions and limitations.

## 2 Numerical formulation

In this section, we present the numerical formulation of a time-dependent fluid-structure interaction problem with thick structure in the case of small displacements, hence the fluid-structure interface is considered as fixed. We consider the incompressible Navier-Stokes equations for the fluid and the Hooke elastic model for the structure.

### 2.1 Governing equations

Referring to Figure 1, we consider a fluid domain  $\Omega^f$  and a structure domain  $\Omega^s$  such that  $\Omega = \Omega^f \cup \Omega^s \subset \mathbb{R}^d$ ,  $d = 2, 3$ , and  $\Sigma = \overline{\Omega^f} \cap \overline{\Omega^s}$  is the fluid-structure interface. We denote by  $\partial\Omega^f$  and  $\partial\Omega^s$  the boundary of the fluid and solid domain, respectively, and we define  $\Gamma^f = \partial\Omega^f \setminus \Sigma$  and  $\Gamma^s = \partial\Omega^s \setminus \Sigma$ . Finally, we indicate with  $\mathbf{n}^f$  and  $\mathbf{n}^s$  the outward unit normal to the domain  $\Omega^f$  and  $\Omega^s$ , respectively. On the interface  $\Sigma$  we have  $\mathbf{n}^f = -\mathbf{n}^s = \mathbf{n}$ .

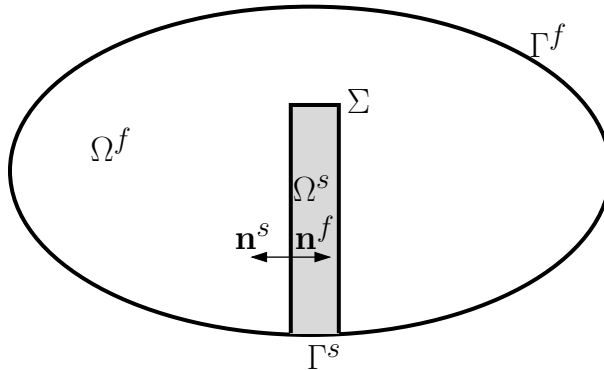


Figure 1: Sketch of the fluid and structure domain  $\Omega^f$  and  $\Omega^s$  with the fluid-structure interface  $\Sigma$ .

The fluid-structure interaction problem reads as follows: find the fluid velocity  $\mathbf{u} : \Omega^f \times (0, T] \rightarrow \mathbb{R}^d$ , the fluid pressure  $p : \Omega^f \times (0, T] \rightarrow \mathbb{R}$ , and the solid

displacement  $\mathbf{d} : \Omega^s \times (0, T] \rightarrow \mathbb{R}^d$ , such that

$$\begin{cases} \rho^f \partial_t \mathbf{u} + \rho^f \mathbf{u} \cdot \nabla \mathbf{u} - \nabla \cdot \mathbf{T}^f(\mathbf{u}, p) = \mathbf{0} & \text{in } \Omega^f \times (0, T], \\ \nabla \cdot \mathbf{u} = 0 & \text{in } \Omega^f \times (0, T], \\ \mathbf{u} = \mathbf{0} & \text{on } \Gamma^f \times (0, T]; \end{cases} \quad (1)$$

$$\begin{cases} \rho^s \partial_{tt} \mathbf{d} - \nabla \cdot \mathbf{T}^s(\mathbf{d}) = \mathbf{0} & \text{in } \Omega^s \times (0, T], \\ \mathbf{d} = \mathbf{0} & \text{on } \Gamma^s \times (0, T]; \end{cases} \quad (2)$$

$$\begin{cases} \mathbf{u} = \dot{\mathbf{d}}, & \text{on } \Sigma \times (0, T], \\ \mathbf{T}^f(\mathbf{u}, p) \mathbf{n}^f = -\mathbf{T}^s(\mathbf{d}) \mathbf{n}^s, & \text{on } \Sigma \times (0, T], \end{cases} \quad (3)$$

where  $T > 0$ ,  $\rho^f$  and  $\rho^s$  are the fluid and structure densities,  $\mathbf{T}^f(\mathbf{u}, p) = -p\mathbf{I} + 2\mu^f \mathbf{D}(\mathbf{u})$  is the fluid Cauchy stress tensor,  $\mathbf{T}^s(\mathbf{d}) = \lambda^s(\nabla \cdot \mathbf{d})\mathbf{I} + 2\mu^s \mathbf{D}(\mathbf{d})$  is the solid stress tensor,  $\mathbf{D}(\mathbf{w}) = \frac{1}{2}(\nabla \mathbf{w} + \nabla \mathbf{w}^T)$ ,  $\mu^f$  is the fluid dynamic viscosity,  $\lambda^s, \mu^s > 0$  are the Lamé parameters,  $\dot{\mathbf{d}} = \partial_t \mathbf{d}$  and where for the sake of simplicity we have considered homogeneous Dirichlet conditions on  $\Gamma^f$  and  $\Gamma^s$ .

The problem is completed with the initial conditions  $\mathbf{u}(\mathbf{x}, 0) = \mathbf{u}^0(\mathbf{x})$ ,  $\mathbf{d}(\mathbf{x}, 0) = \mathbf{d}^0(\mathbf{x})$  and  $\dot{\mathbf{d}}(\mathbf{x}, 0) = \mathbf{v}^0(\mathbf{x})$ .

## 2.2 Spatial discretization

We consider the spaces  $\mathbf{V} = [H_{\Gamma^f}^1(\Omega^f)]^d$ ,  $Q = L^2(\Omega^f)$  and  $\mathbf{W} = [H_{\Gamma^s}^1(\Omega^s)]^d$ , where  $H_{\Gamma^f}^1(\Omega^f) = \{v \in H^1(\Omega^f), v|_{\Gamma^f} = 0\}$  and  $H_{\Gamma^s}^1(\Omega^s) = \{v \in H^1(\Omega^s), v|_{\Gamma^s} = 0\}$ . The weak formulation of the problem given by (1)-(3) reads as follows: for  $t \in (0, T]$ , find  $(\mathbf{u}(t), p(t), \mathbf{d}(t)) \in \mathbf{V} \times Q \times \mathbf{W}$  such that  $\mathbf{u} = \dot{\mathbf{d}}$  on  $\Sigma$ , and

$$\begin{cases} \rho^f (\partial_t \mathbf{u}, \mathbf{v})_{\Omega^f} + a^f(\mathbf{u}, \mathbf{v}) + b(p, \mathbf{v}) - b(q, \mathbf{u}) + c(\mathbf{u}, \mathbf{u}, \mathbf{v}) \\ + \rho^s (\partial_{tt} \mathbf{d}, \mathbf{w})_{\Omega^s} + a^s(\mathbf{d}, \mathbf{w}) = 0, \end{cases}$$

for all  $(\mathbf{v}, q, \mathbf{w}) \in \mathbf{V} \times Q \times \mathbf{W}$  such that  $\mathbf{v}|_{\Sigma} = \mathbf{w}|_{\Sigma}$ . Here, with  $\cdot|_{\Sigma}$  we indicate the trace on  $\Sigma$  and we have indicated by  $(\cdot, \cdot)_{\Omega^i}$ ,  $i = f, s$ , the  $L^2$  product over  $\Omega^i$ . Moreover, we have introduced the bi-linear forms  $a^f : \mathbf{V} \times \mathbf{V} \rightarrow \mathbb{R}$ ,  $b : Q \times \mathbf{V} \rightarrow \mathbb{R}$  and  $a^s : \mathbf{W} \times \mathbf{W} \rightarrow \mathbb{R}$  defined as

$$a^f(\mathbf{u}, \mathbf{v}) = 2\mu^f (\mathbf{D}(\mathbf{u}), \mathbf{D}(\mathbf{v}))_{\Omega^f},$$

$$b(p, \mathbf{v}) = -(p, \nabla \cdot \mathbf{v})_{\Omega^f},$$

$$a^s(\mathbf{d}, \mathbf{w}) = \lambda^s (\nabla \cdot \mathbf{d}, \nabla \cdot \mathbf{w})_{\Omega^s} + 2\mu^s (\mathbf{D}(\mathbf{d}), \mathbf{D}(\mathbf{w}))_{\Omega^s},$$

and the tri-linear form  $c : \mathbf{V} \times \mathbf{V} \times \mathbf{V} \rightarrow \mathbb{R}$  defined as

$$c(\mathbf{z}, \mathbf{u}, \mathbf{v}) = \rho^f (\mathbf{z} \cdot \nabla \mathbf{u}, \mathbf{v})_{\Omega_f}.$$

To ease the presentation, we assume that  $\Omega^f$ ,  $\Omega^s$  and  $\Sigma$  are polyhedral. We denote by  $\mathcal{T}_h^s$  the solid mesh that covers the domain  $\Omega^s$  and it is fitted to  $\partial\Omega^s$  and by  $\mathcal{T}_h^f$  the fluid mesh that covers the whole domain  $\Omega$  and it is fitted to  $\Gamma^f$ , but in general not to  $\Sigma$  and  $\Gamma^s$ . We indicate with  $h > 0$  the spatial discretization step. As result, the solid mesh  $\mathcal{T}_h^s$  overlaps the fluid mesh  $\mathcal{T}_h^f$ , see Figure 2. We

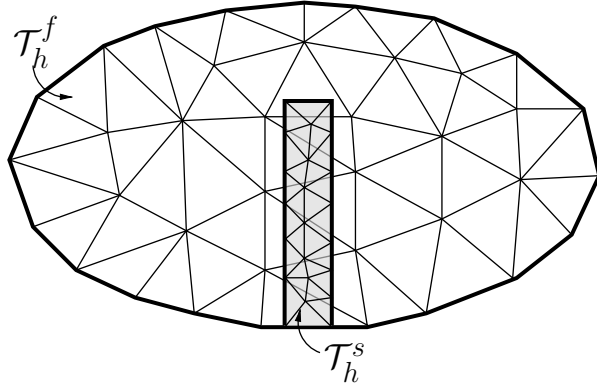


Figure 2: The structure mesh  $\mathcal{T}_h^s$  overlaps the fluid mesh  $\mathcal{T}_h^f$ .

also introduce the following mesh

$$\mathcal{G}_h = \{K : K \in \mathcal{T}_h^f, K \cap \Sigma \neq \emptyset, K \cap \Omega^f \text{ is a disconnected set}\},$$

that consists of all the elements  $K$  in  $\mathcal{T}_h^f$  cut by the interface  $\Sigma$  such that they are split elements, i.e., each fluid element  $K$  is split into two or more fluid subparts, see Figure 3 (left). In general, a split element  $K$  may be divided into  $N^K$  fluid subparts, see Figure 3 (right). We define  $\mathcal{G}_h^P$  the collection of all connected subset of  $K \cap \Omega^f$ , for all  $K \in \mathcal{G}_h$ . More precisely

$$P \in \mathcal{G}_h^P \iff \exists K \in \mathcal{G}_h \text{ s.t. } P \subset K \cap \Omega^f, P \text{ is a connected set.}$$

The set  $\mathcal{G}_h^P$  can be partitioned by identifying the maximal connected sets found by the union of elements of  $\mathcal{G}_h^P$ , more precisely we can identify  $N^f$  subsets of  $\bar{\Omega}^f$ ,  $\Omega_h^i$ ,  $i = 1, \dots, N^f$ , so that

$$\begin{aligned} &\Omega_h^i \text{ is connected, } \Omega_h^i \subset \bigcup_{P \in \mathcal{G}_h^P} P \text{ and} \\ &\text{if } P \cap \bar{\Omega}_h^i = \emptyset \implies P \cup \Omega_h^i \text{ is a disconnected set, } \forall P \in \mathcal{G}_h^P, \end{aligned}$$

see Figure 4 (left). Given any element  $K \in \mathcal{G}_h$  we can now number its fluid subparts according to which  $\Omega_h^i$  they belong. We call  $P_i^K$  the set that satisfies

$$P_i^K \subset K \cap \Omega^f, P_i^K \subset \Omega_h^i,$$

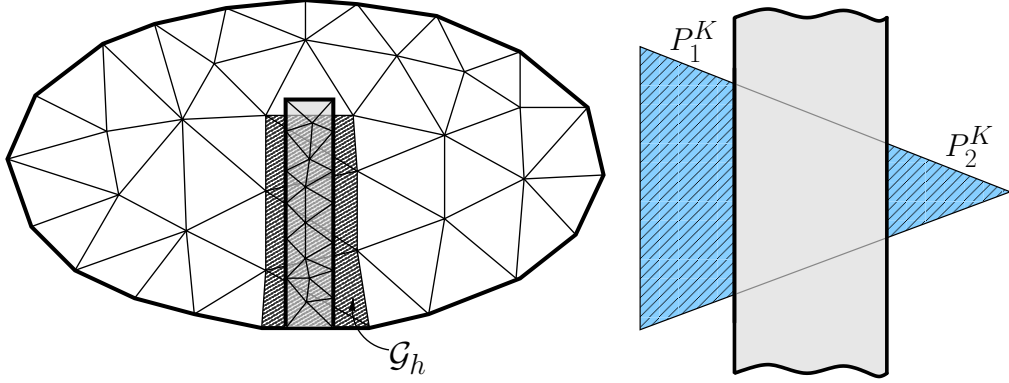


Figure 3: Left: representation of the mesh  $\mathcal{G}_h$ . Right: representation of a split element  $K$  with two fluid subparts  $P_1^K$  and  $P_2^K$ .

see Figure 3 (right).

Moving from these definitions, we set

$$\Omega_h^0 = \Omega^f \setminus \bigcup_{K \in \mathcal{G}_h} K,$$

see Figure 4 (left), and we denote by  $\mathcal{T}_h^0$  the smallest mesh composed of the elements  $K \in \mathcal{T}_h^f$  that covers the set  $\Omega_h^0$ , i.e.,

$$K \in \mathcal{T}_h^0 \iff K \cap \bar{\Omega}_h^0 \neq \emptyset$$

see Figure 4 (right). Finally, we denote by  $\mathcal{T}_h^i$ , for  $i = 1, \dots, N^f$ , the smallest mesh that consists of all the elements of  $\mathcal{G}_h$  that covers the set  $\Omega_h^i$ , i.e.,

$$K \in \mathcal{T}_h^i \iff K \cap \bar{\Omega}_h^i \neq \emptyset, \quad i = 1, \dots, N^f.$$

In this way, each element  $K \in \mathcal{G}_h$  belongs to  $N^K$  different meshes  $\mathcal{T}_h^i$ . We point out that  $\Omega^f = \bigcup_{i=0, \dots, N^f} \Omega_h^i$  and that  $\Omega_h^i \cap \Omega_h^j = \emptyset, \forall i \neq j$ . We observe that the set covered by  $\mathcal{T}_h^i$  is larger than the one covered by the corresponding  $\Omega_h^i$ , see Figure 4 (right). It is important to distinguish between the physical parts  $\Omega_h^i$  and the computational ones  $\mathcal{T}_h^i$ , since some operators act on the former, while other operators, such as the stabilization terms, on the latter. This requires to be able to integrate over a portion of an element  $K$  or a portion of a facet  $F$ . A detailed explanation of this point will be presented in Section 3. In what follows, we indicate with

- *physical*, the restriction of a geometrical entity of  $\mathcal{T}_h^i$  on  $\Omega_h^i$ ;
- *computational*, the entire geometrical entity in the mesh  $\mathcal{T}_h^i$ .

To ease the presentation, in what follows we suppose that  $N^f = 2$ , so that we have only the sets  $\Omega_h^1$  and  $\Omega_h^2$ , see Figure 4 (left).

Thanks to the above definitions, we denote by

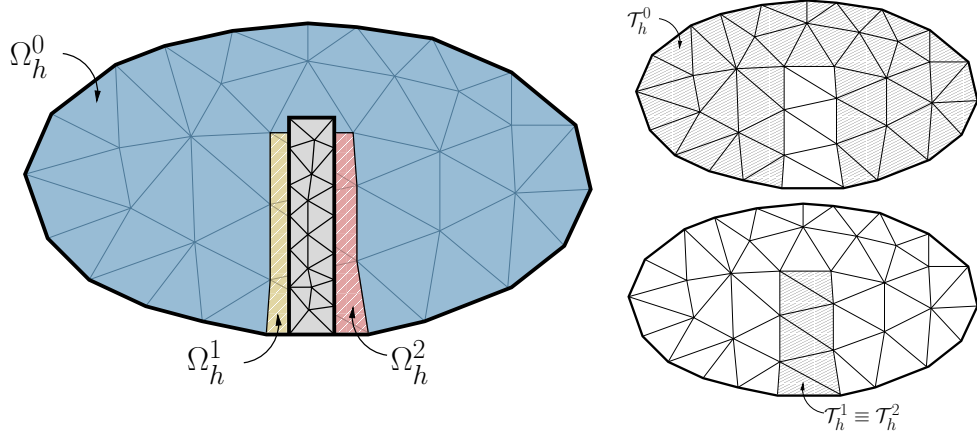


Figure 4: Left: sketch of the sets  $\Omega_h^0$ ,  $\Omega_h^1$  and  $\Omega_h^2$  in the case of  $N^f = 2$ . Right: the shaded regions represent the meshes  $\mathcal{T}_h^0$  (top) and  $\mathcal{T}_h^i$  (bottom) in the case of  $N^f = 2$ . In this case,  $\mathcal{T}_h^1$  coincides with  $\mathcal{T}_h^2$ .

- $\mathcal{F}_{h,phy}^i$ , the physical part of the faces in  $\mathcal{T}_h^i$ ,  $i = 1, 2$ , see Figure 5(a), on which we weakly impose the continuity of the fluid velocity and stresses by means of the DG formulation;
- $\mathcal{F}_{h,com}^i$ , the computational counterpart of the faces  $\mathcal{F}_{h,phy}^i$ ,  $i = 1, 2$ , see Figure 5(b)-(c);
- $\mathcal{F}_{h,\Sigma}^i$ , the (computational) faces of  $\mathcal{T}_h^i$ ,  $i = 1, 2$ , cut by the interface  $\Sigma$ , see Figure 5(d).

As we will explain in Section 3.3, the degrees of freedom associated to the elements in  $\mathcal{G}_h$  are duplicated according to the XFEM strategy: a set of degrees of freedom is used to compute the solution over  $\mathcal{T}_h^1$ , and a second set of degrees of freedom is used to compute the solution over  $\mathcal{T}_h^2$ . In the case the number of fluid subparts shared by the common face  $F$  of two elements  $K_1 \in \mathcal{T}_h^0$  and  $K_2 \in \mathcal{G}_h$  is not equal, it is not possible to apply continuity at the interface strongly, see for example Figure 4 (left), where the fluid element near the tip of the structure (in blue) faces two fluid subparts (in yellow and red). For this reason, we apply a DG mortaring on these interfaces and, for simplicity, on all faces that belongs to  $\mathcal{F}_{h,phy}^i$ , for  $i = 1, 2$ .

We introduce the following spaces:

$$X_h^f = \{v_h \in L^2(\Omega^f) : v_h \in C^0(\Omega_h^0), v_h|_K \in \mathbb{P}_1(K), \forall K \in \mathcal{T}_h^i \text{ for } i = 0, 1, 2\},$$

and

$$X_h^s = \{v_h \in C^0(\bar{\Omega}^s) : v_h|_K \in \mathbb{P}_1(K), \forall K \in \mathcal{T}_h^s\}.$$

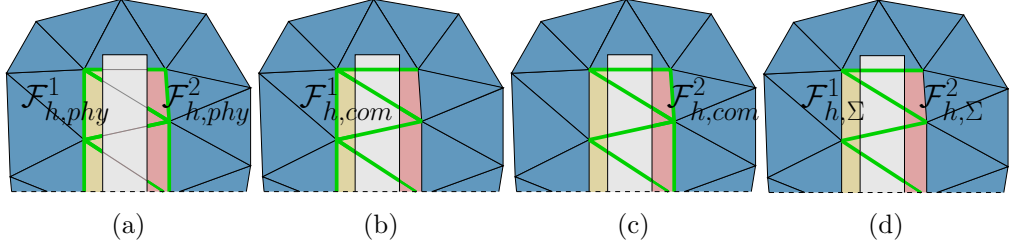


Figure 5: Representation of the sets of faces involved in the integration (highlighted in green): (a) the physical faces  $\mathcal{F}_{h,phy}^1$  and  $\mathcal{F}_{h,phy}^2$ ; (b) the computational faces  $\mathcal{F}_{h,com}^1$ ; (c) the computational faces  $\mathcal{F}_{h,com}^2$ ; (d) the computational faces  $\mathcal{F}_{h,\Sigma}^1$  and  $\mathcal{F}_{h,\Sigma}^2$  intersected by  $\Sigma$  which, in this example, coincide.

For the approximation of the fluid velocity, fluid pressure and solid displacement we consider the spaces

$$\mathbf{V}_h = \{\mathbf{v}_h \in [X_h^f]^d : \mathbf{v}_h|_{\Gamma^f} = 0\}, \quad Q_h = \{q_h \in X_h^f\},$$

$$\mathbf{W}_h = \{\mathbf{w}_h \in [X_h^{s1}]^d : \mathbf{w}_h|_{\Gamma^s} = 0\},$$

respectively.

Further, we introduce some trace operators defined over an interface  $\mathcal{I}$  that separates a domain  $\Omega_{1,2}$  into  $\Omega_1$  and  $\Omega_2$ , such that  $\bar{\Omega}_{1,2} = \bar{\Omega}_1 \cup \bar{\Omega}_2$  and  $\bar{\Omega}_1 \cap \bar{\Omega}_2 = \mathcal{I}$ . For a function  $q$ , we denote by  $[[\cdot]]_{\mathcal{I}}$  the jump and by  $\{\{\cdot\}\}_{\mathcal{I},\alpha}$  the  $\alpha$ -weighted mean across the interface  $\mathcal{I}$ , defined as

$$[[q]]_{\mathcal{I}} = q_1 - q_2, \quad \{\{q\}\}_{\mathcal{I},\alpha} = \alpha q_1 + (1 - \alpha) q_2, \quad (4)$$

where  $q_1$  and  $q_2$  are the traces of  $q$  at the two sides of the interface and  $\alpha \in [0, 1]$ . If the subscript  $\alpha$  is not indicated, we assume that  $\alpha = \frac{1}{2}$ .

The space semi-discretization problem related to (1)-(3) reads as follows: for

$t \in (0, T]$ , given  $\beta > 0$ , find  $(\mathbf{u}_h(t), p_h(t), \mathbf{d}_h(t)) \in \mathbf{V}_h \times Q_h \times \mathbf{W}_h$  such that

$$\left\{ \begin{array}{l} \rho^f (\partial_t \mathbf{u}_h, \mathbf{v}_h)_{\Omega^f} + a^f(\mathbf{u}_h, \mathbf{v}_h) + b(p_h, \mathbf{v}_h) - b(q_h, \mathbf{u}_h) + c(\mathbf{u}_h, \mathbf{u}_h, \mathbf{v}_h) \\ + \rho^s (\partial_{tt} \mathbf{d}_h, \mathbf{w}_h)_{\Omega^s} + a^s(\mathbf{d}_h, \mathbf{w}_h) \\ + c_h(\mathbf{u}_h, \mathbf{u}_h, \mathbf{v}_h) + s_h^p(p_h, q_h) + g_h(\mathbf{u}_h, \mathbf{v}_h) \\ - (\alpha \mathbf{T}^f(\mathbf{u}_h, p_h) \mathbf{n}^f + (1 - \alpha) \mathbf{T}^s(\mathbf{d}_h) \mathbf{n}^f, \mathbf{v}_h - \mathbf{w}_h)_\Sigma \\ - (\mathbf{u}_h - \dot{\mathbf{d}}_h, \alpha \mathbf{T}^f(\mathbf{v}_h, -q_h) \mathbf{n}^f + (1 - \alpha) \mathbf{T}^s(\mathbf{w}_h) \mathbf{n}^f)_\Sigma \\ + \frac{\gamma_\Sigma \mu^f}{h} (\mathbf{u}_h - \dot{\mathbf{d}}_h, \mathbf{v}_h - \mathbf{w}_h)_\Sigma \\ - \sum_{i=1,2} \sum_{F \in \mathcal{F}_{h,phy}^i} \left( \{ \{ \mathbf{T}^f(\mathbf{u}_h, p_h) \} \}_{F,\beta} \mathbf{n}^f, \llbracket \mathbf{v}_h \rrbracket_F \right)_F \\ - \sum_{i=1,2} \sum_{F \in \mathcal{F}_{h,phy}^i} \left( \llbracket \mathbf{u}_h \rrbracket_F, \{ \{ \mathbf{T}^f(\mathbf{v}_h, -q_h) \} \}_{F,\beta} \mathbf{n}^f \right)_F \\ + \sum_{i=1,2} \sum_{F \in \mathcal{F}_{h,phy}^i} \frac{\gamma_{phy}^v \mu^f}{h_F} (\llbracket \mathbf{u}_h \rrbracket_F, \llbracket \mathbf{v}_h \rrbracket_F)_F = 0, \end{array} \right. \quad (5)$$

for all  $(\mathbf{v}_h, q_h, \mathbf{w}_h) \in \mathbf{V}_h \times Q_h \times \mathbf{W}_h$ . We have indicated by  $\gamma_\Sigma > 0$  and  $\gamma_{phy}^v > 0$  the penalty parameters related to the interface  $\Sigma$  and to the faces in  $\mathcal{F}_{h,phy}^i$ , respectively. In (5), we have introduced:

- a Brezzi-Pitkäranta-type pressure stabilization, see, e.g., [6, 9], defined as

$$\begin{aligned} s_h^p(p_h, q_h) &= \gamma_p \sum_{i=0,1,2} \sum_{K \in \mathcal{T}_h^i} \frac{h_K^2}{\mu^f} \int_K \nabla p_h \cdot \nabla q_h \\ &+ \gamma_{com}^p \sum_{i=1,2} \sum_{F \in \mathcal{F}_{h,com}^i} \frac{h_F}{\mu^f} \int_F \llbracket p_h \rrbracket_F \cdot \llbracket q_h \rrbracket_F, \end{aligned}$$

with  $\gamma_p > 0$  and  $\gamma_{com}^p > 0$  the penalty parameters related to the pressure stabilization on  $\mathcal{T}_h^i$ ,  $i = 0, 1, 2$ , and the pressure stabilization on the faces in  $\mathcal{F}_{h,com}^i$ , respectively;

- a ghost-penalty term, see [7], to guarantee robustness of the method w.r.t. the cut elements, defined as

$$g_h(\mathbf{u}_h, \mathbf{v}_h) = \gamma_g \sum_{i=1,2} \sum_{F \in \mathcal{F}_{h,\Sigma}^i} \mu^f h_F \int_F \llbracket \nabla \mathbf{u}_h \rrbracket_F \mathbf{n} \cdot \llbracket \nabla \mathbf{v}_h \rrbracket_F \mathbf{n},$$

with  $\gamma_g > 0$ ;

- a correction of the convective term to maintain the condition  $c(\mathbf{z}, \mathbf{v}, \mathbf{v}) = 0, \forall \mathbf{v} \in \mathbf{V}, \mathbf{z} \in \{\mathbf{v} \in \mathbf{V}, \nabla \cdot \mathbf{v} = 0\}$  in the discrete space, see [33, 12], defined

as

$$\begin{aligned}
c_h(\mathbf{z}_h, \mathbf{u}_h, \mathbf{v}_h) &= \frac{\rho^f}{2} ((\nabla \cdot \mathbf{z}_h) \mathbf{u}_h, \mathbf{v}_h)_{\Omega^f} \\
&\quad - \sum_{i=1,2} \sum_{F \in \mathcal{F}_{h,phy}^i} \rho^f \left( \{\{\mathbf{z}_h\}\}_{F,\alpha} \cdot \mathbf{n} \llbracket \mathbf{u}_h \rrbracket_F, \{\{\mathbf{v}_h\}\}_{F,\alpha} \right)_F \\
&\quad - \frac{\rho^f}{2} (\mathbf{z}_h \cdot \mathbf{n}, \mathbf{u}_h \cdot \mathbf{v}_h)_{\Sigma}.
\end{aligned}$$

### 2.3 Full discretization

We denote by  $\Delta t > 0$  the temporal discretization step and by  $(0, T]$  the temporal domain such that  $t^n = n\Delta t$ , for  $n = 1, \dots, N_t$  with  $N_t = \frac{T}{\Delta t}$ . To ease the presentation, we consider only the backward difference formula (BDF) of order 1 for the time discretization. The space-time discretization of the problem given by (1)-(3) reads as follows: for  $n = 0, \dots, N_t - 1$ , find  $(\mathbf{u}_h^{n+1}, p_h^{n+1}, \mathbf{d}_h^{n+1}) \in \mathbf{V}_h \times Q_h \times \mathbf{W}_h$  such that

$$\left\{ \begin{aligned}
&\frac{\rho^f}{\Delta t} (\mathbf{u}_h^{n+1}, \mathbf{v}_h)_{\Omega^f} + a^f(\mathbf{u}_h^{n+1}, \mathbf{v}_h) + b(p_h^{n+1}, \mathbf{v}_h) - b(q_h, \mathbf{u}_h^{n+1}) + c(\mathbf{u}_h^n, \mathbf{u}_h^{n+1}, \mathbf{v}_h) \\
&+ \frac{\rho^s}{\Delta t^2} (\mathbf{d}_h^{n+1}, \mathbf{w}_h)_{\Omega^s} + a^s(\mathbf{d}_h^{n+1}, \mathbf{w}_h) \\
&+ c_h(\mathbf{u}_h^n, \mathbf{u}_h^{n+1}, \mathbf{v}_h) + s_h^p(p_h^{n+1}, q_h) + g_h(\mathbf{u}_h^{n+1}, \mathbf{v}_h) \\
&- (\alpha \mathbf{T}^f(\mathbf{u}_h^{n+1}, p_h^{n+1}) \mathbf{n}^f + (1 - \alpha) \mathbf{T}^s(\mathbf{d}_h^{n+1}) \mathbf{n}^f, \mathbf{v}_h - \mathbf{w}_h)_{\Sigma} \\
&- \left( \mathbf{u}_h^{n+1} - \frac{\mathbf{d}_h^{n+1}}{\Delta t}, \alpha \mathbf{T}^f(\mathbf{v}_h, -q_h) \mathbf{n}^f + (1 - \alpha) \mathbf{T}^s(\mathbf{w}_h) \mathbf{n}^f \right)_{\Sigma} \\
&+ \frac{\gamma_{\Sigma} \mu^f}{h} \left( \mathbf{u}_h^{n+1} - \frac{\mathbf{d}_h^{n+1}}{\Delta t}, \mathbf{v}_h - \mathbf{w}_h \right)_{\Sigma} \\
&- \sum_{i=1,2} \sum_{F \in \mathcal{F}_{h,phy}^i} \left( \{\{\mathbf{T}^f(\mathbf{u}_h^{n+1}, p_h^{n+1})\}\}_{F,\beta} \mathbf{n}^f, \llbracket \mathbf{v}_h \rrbracket_F \right)_F \\
&- \sum_{i=1,2} \sum_{F \in \mathcal{F}_{h,phy}^i} \left( \llbracket \mathbf{u}_h^{n+1} \rrbracket_F, \{\{\mathbf{T}^f(\mathbf{v}_h, -q_h)\}\}_{F,\beta} \mathbf{n}^f \right)_F \\
&+ \sum_{i=1,2} \sum_{F \in \mathcal{F}_{h,phy}^i} \frac{\gamma_{phy}^v \mu^f}{h_F} \left( \llbracket \mathbf{u}_h^{n+1} \rrbracket_F, \llbracket \mathbf{v}_h \rrbracket_F \right)_F = \\
&\frac{\rho^f}{\Delta t} (\mathbf{u}_h^n, \mathbf{v}_h)_{\Omega^f} + \frac{2\rho^s}{\Delta t^2} (\mathbf{d}_h^n, \mathbf{w}_h)_{\Omega^s} + \frac{\rho^s}{\Delta t^2} (\mathbf{d}_h^{n-1}, \mathbf{w}_h)_{\Omega^s} \\
&+ \left( \frac{\mathbf{d}_h^n}{\Delta t}, \alpha \mathbf{T}^f(\mathbf{v}_h, -q_h) \mathbf{n}^f + (1 - \alpha) \mathbf{T}^s(\mathbf{w}_h) \mathbf{n}^f \right)_{\Sigma} - \frac{\gamma_{\Sigma} \mu^f}{h} \left( \frac{\mathbf{d}_h^n}{\Delta t}, \mathbf{v}_h - \mathbf{w}_h \right)_{\Sigma},
\end{aligned} \right. \quad (6)$$

for all  $(\mathbf{v}_h, q_h, \mathbf{w}_h) \in \mathbf{V}_h \times Q_h \times \mathbf{W}_h$ , and where we have used a first order extrapolation to treat the non-linearity of the convective term.

The algebraic linear system associated with equation (6) reads:

$$RU = \mathbf{F}$$

where

$$R = \begin{bmatrix} K^f + C(\mathbf{U}^n) + G + E^{\mathbf{uu}} + H^{\mathbf{uu}} & B^T + E^{\mathbf{up}} + H^{\mathbf{up}} & E^{\mathbf{ud}} \\ -B + E^{\mathbf{up}T} + H^{\mathbf{up}T} & S & E^{\mathbf{dp}} \\ E^{\mathbf{ud}T} & E^{\mathbf{dp}T} & K^s + E^{\mathbf{dd}} \end{bmatrix},$$

$$\mathbf{U} = \begin{bmatrix} \mathbf{U}^{n+1} \\ \mathbf{P}^{n+1} \\ \mathbf{D}^{n+1} \end{bmatrix} \quad \text{and} \quad \mathbf{F} = \begin{bmatrix} \mathbf{F}_u \\ \mathbf{F}_p \\ \mathbf{F}_d \end{bmatrix}.$$

We have indicated by  $K^f = \Delta t^{-1}M^f + A^f$  and  $K^s = \Delta t^{-2}M^s + A^s$ , where  $M^f, A^f, B$  and  $C(\mathbf{U}^n)$  represent the standard matrices of the Finite Element discretization of the Navier-stokes problem,  $M^s$  and  $A^s$  represent the mass and stiffness matrices related to the structure discretization,  $S$  the matrix related to the fluid stabilization and  $G$  the matrix associated with the ghost penalty term. The matrices  $E$  contain the DG terms that couple the fluid and the structure on the interface  $\Sigma$ , while the matrices  $H$  contain the DG terms that ensure the weak continuity of the velocity and stresses on the faces  $\mathcal{F}_{h,phy}^i$ .

### 3 Implementation details

In this section, we describe the main issues that arise during the implementation of the proposed XFEM/DG approach, in particular the specific features that characterize the method with respect to the standard Finite Element Method.

In what follows, we indicate with

- *background* mesh, the fluid mesh  $\mathcal{T}_h^f$  that covers the entire domain;
- *foreground* mesh, the solid mesh  $\mathcal{T}_h^s$  that covers the solid domain and overlaps the fluid one;
- *cut-entities*, the physical portion of the geometrical entities of the background mesh partially covered by the foreground mesh, which, in the case of volumes or faces, are in general polyhedra or polygon, see Figure 6 (left). In particular, we refer to *cut-elements* and *cut-faces* the case of three-dimensional and two-dimensional entities;
- *cut-mesh*, the fluid mesh resulting from the difference between the background mesh and the foreground one, see Figure 6 (right), that coincides with the physical portion of the background mesh (i.e. the union of cut-entities and the elements not covered by the foreground mesh), in the sense of the definition given in Section 2.2.

Due to the unfitted nature of the involved meshes, it is necessary to identify which parts of the entities in the background mesh are physical (i.e. belonging to the cut-mesh) with the aim of computing the integrals over these portions. The main steps to address are:

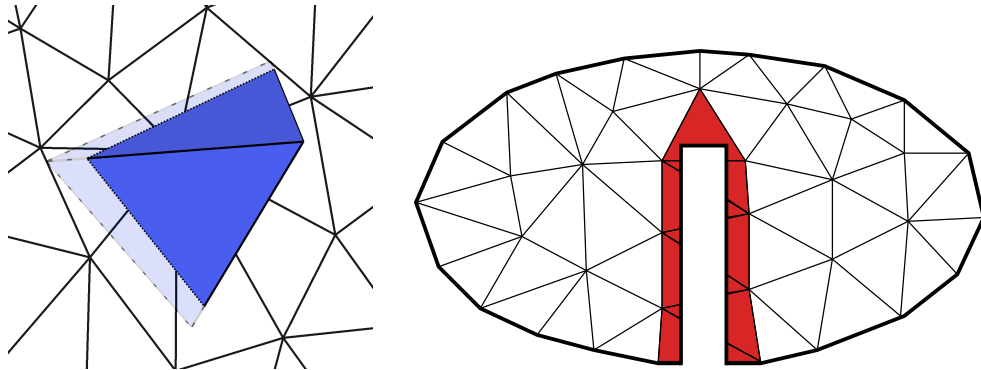


Figure 6: Left: example of a tetrahedron (blue) of the background mesh that intersects the interface  $\Sigma$  (white mesh). The darker part represents the physical part given by the cut-element, i.e., the portion of the element that is not overlapped by the foreground mesh, while the lighter part is the overlapped one. Right: the cut-mesh associated with the background mesh shown in Figure 2 that contains cut-elements (in red).

1. the computation of the intersections between the unfitted meshes;
2. the generation of the cut-elements and cut-mesh;
3. the addition of the extended degrees of freedom according to the XFEM philosophy;
4. the integration over the cut-elements and cut-faces.

### 3.1 Intersection between meshes

To identify the physical portions of the cut-entities it is necessary to compute the intersection points between the background and foreground mesh. These intersections will be used to reconstruct the cut-elements and the cut-faces on the interface.

Referring to Figure 7, we show two configurations where the intersections points between the background and interface meshes are represented: to the left, we consider the case of an element with only one fluid physical element, while to the right we consider the case of two fluid physical elements. The computation of the intersections points may be very expensive from a computational viewpoint, since it is not known a-priori which elements of the background mesh are intersected, so a naive procedure may be to check all the elements of the foreground mesh for each element of the background mesh. To avoid this and to obtain an efficient algorithm, we rely on an Alternating Digital Tree (ADTree), see [4, 14]. This data structure, given a bounding box of an entity of the foreground mesh, allows to check if the bounding box intersects the elements of background mesh and returns a list of these elements. Once the list is obtained,

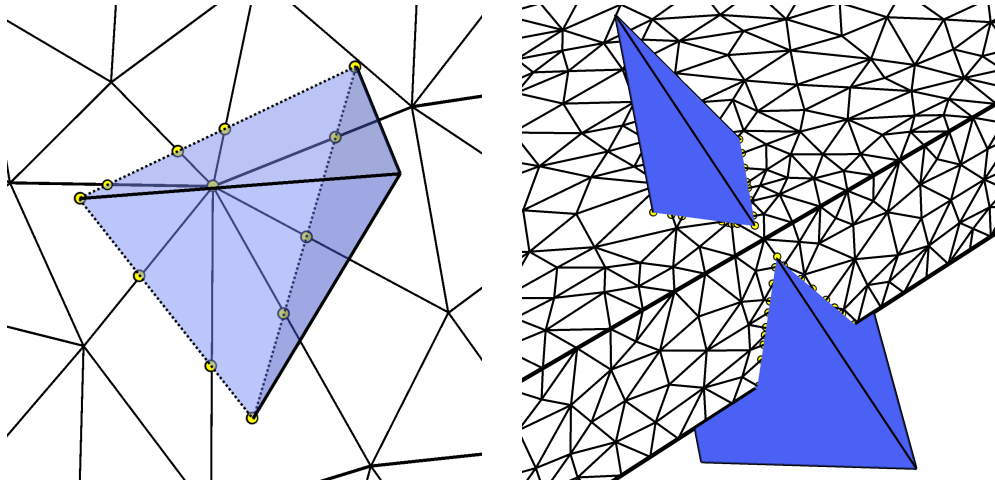


Figure 7: The foreground mesh (in white) and the physical part of the tetrahedron (in blue). The resulting intersection points are highlighted (in yellow). Left: one fluid physical element is generated. Right: two fluid physical elements are generated.

we proceed to compute the intersection points. A similar strategy has been already employed, for example, in [23].

At the end of this procedure, for each element of the background mesh that is cut by the foreground one, we have a list of all the intersection points.

### 3.2 Generation of the cut-mesh

The intersection points calculated are stored to generate a sub-tetrahedralization inside each element of the background mesh. The purpose of this tetrahedralization is twofold: i) it will be used to integrate over the cut-elements and the cut-faces, ii) it will be used to visualize the numerical solution. The first point will be explained in detail in Section 3.4. Regarding the second one, the sub-tetrahedralizations are employed to visualize the solution only on the cut-mesh instead on the entire background mesh, by avoiding the visualization of the solution on the non-physical portions of the elements.

The sub-tetrahedralization has to fulfill two requirements: i) we have to force the intersection points to be vertices of the final tetrahedralization; ii) the possible additional vertices introduced by the tetrahedralization has to lie inside the element, otherwise the conformity between facing element will be lost. To satisfy these requirements, for each element  $K$ , we proceed as follows:

1. a one-dimensional mesh for each edge of  $K$  is generated by using the intersection points that lie on the edge as vertices, see Figure 8 (left-center);
2. a two-dimensional mesh for each face of  $K$  is generated by using the edges computed at step 1 to define the boundary of the face, and by using the

intersection points that lie of the face as vertices, see Figure 8 (center-right);

3. a three-dimensional mesh is generated by using the faces computed at step 2 to define the boundary of the element, and by using the intersection points that lie inside the volume of the element.

Steps 2 and 3 are carried out by Triangle [29] and TetGen [30], respectively. In Figure 9, we report the sub-tetrahedralization for the cases presented in Figure 7.

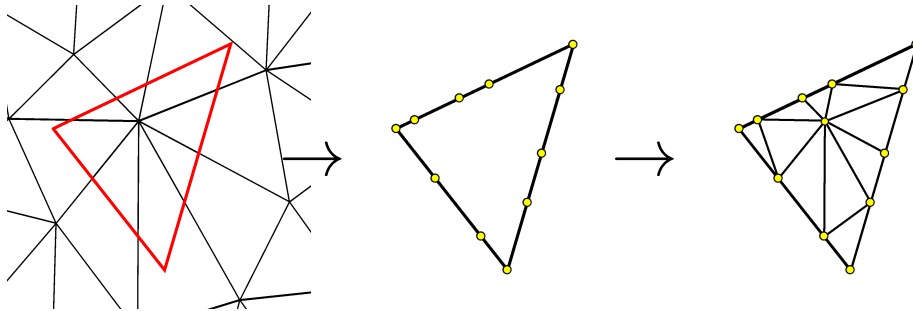


Figure 8: Sub-triangulation of the face of the element in Figure 7. Left: face of the background mesh (in red) and the foreground mesh (in white). Center: generation of the one-dimensional meshes over the edges. Right: generation of the two-dimensional mesh over the face. The intersection points are highlighted in yellow.

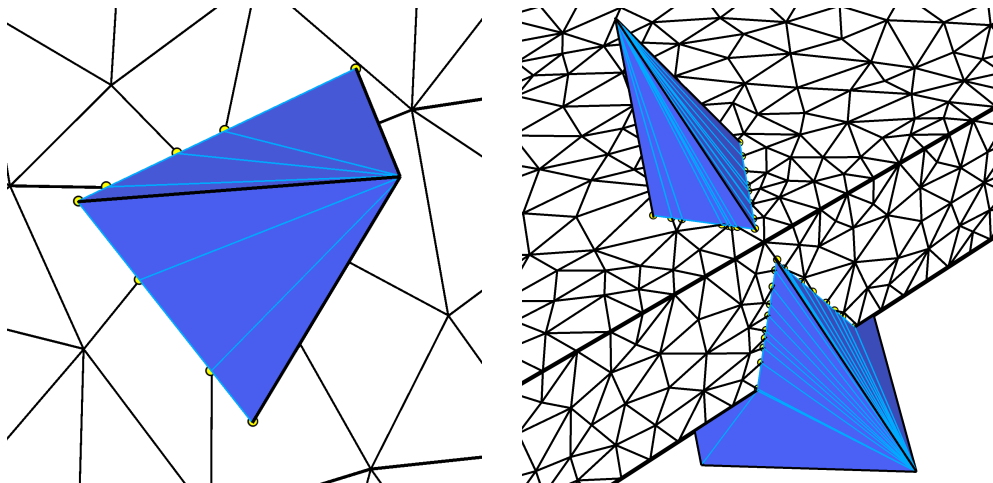


Figure 9: Tetrahedralization of the element, with the edges of the sub-tetrahedra highlighted in light blue. Left: element with one fluid physical element. Right: element with two fluid physical elements.

### 3.3 Extended degrees of freedom

The main goal of the tetrahedralization is the computation of the integrals over the cut-entities. To this aim, it is first necessary to identify which degrees of freedom (dofs) need to be selected when integrating an element of the background mesh. To ease the presentation, in what follows we refer to the dofs associated with conforming piecewise linear finite element.

The elements of the background mesh can be divided into three categories:

- elements that are non-overlapped by the foreground mesh, see Figure 10 (left). In this case, we select the dofs of the standard FEM and integration proceeds as usual;
- elements that are partially-overlapped by the foreground mesh, see Figure 10 (center). In this case, we may have to consider additional dofs depending on the number of physical elements as explained below;
- elements that are fully-overlapped by the foreground mesh, see Figure 10 (right). In this case, we do not have to consider any dof on the element since the latter does not belong to the physical domain.

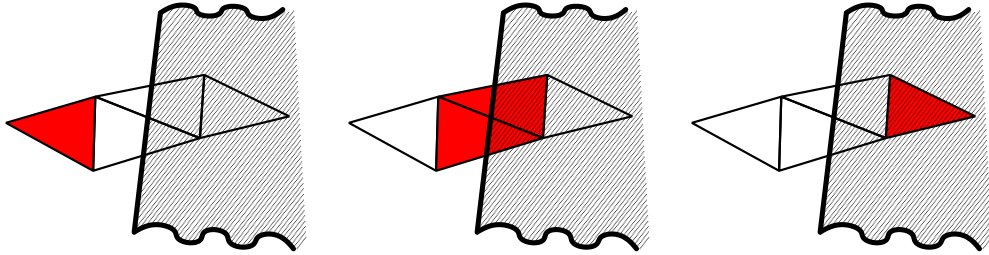


Figure 10: Possible scenarios of background elements (in red) with respect to the foreground mesh (in grey). From left to right: the element is not overlapped, the two elements are partially overlapped, the element is completely overlapped.

As shown in the previous section, the case of partially-overlapped element generates many possible configurations: an element cut into only one physical part (see Figure 9, left), an element cut into two physical parts (see Figure 9, right), and an element cut into more physical parts. The latter case can be treated analogously to the case of two subparts, so that we discuss here only the first two cases. In the case of only one fluid physical part, we just consider the standard dofs of the FEM, see Figure 11 (left). In the case of two fluid physical elements, we have to double the finite element, i.e., the geometric entity and its associated dofs, see Figure 11 (right). Hence, we will use a first set of dofs to compute the integrals over one physical element, and the second set of dofs to compute the integrals over the other physical element, see, e.g. [19]. As noticed in Section 2, these additional dofs needs to be coupled with the surrounding ones

to achieve continuity of the solution. To do this, we impose a DG mortaring to weakly impose the continuity of the solution.

We notice that a similar strategy to handle the FSI problem for unfitted meshes in the case of thick structure has been studied in [8] as well. However, in that paper the authors do not consider that a fluid element could be cut by the solid into two physical parts, and thus they do not need to double the dofs. In some sense our approach is similar to that proposed in [28] even if in this paper the authors consider only a fluid problem, not a FSI one.

In the next section, we show how to perform the numerical integration in such cases.

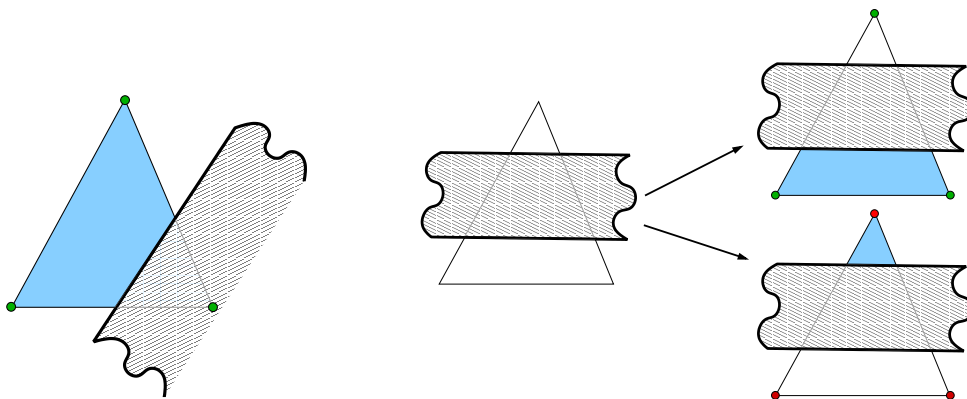


Figure 11: The two main configurations that may appear in the case of partially-overlapped elements. Left: case of one physical element (in blue), the foreground mesh (in grey) and the dofs highlighted in green. Right: case of two physical elements with the background element (in white) and the foreground mesh (in grey). In this case, the set of dofs are doubled (in green and red) and each set it is used to compute the solution only in one of the two physical element (in blue).

### 3.4 Integration over cut-entities

The integration over the physical portions of the partially-overlapped elements, that, in general, are complex polyhedra, requires to consider advanced numerical integration techniques. Some of these techniques are presented, e.g., in [26, 25, 32, 35].

To avoid implementing new numerical quadrature formula and to reuse the classical Gaussian quadrature rule available in a standard FEM implementation, we proceed instead as follows: by using the tetrahedralization generated inside each partially-overlapped element, we compute the integral over each sub-tetrahedron and then we sum up all the contributions.

By referring to the configurations shown in Figure 12:

- in the case of one physical part (left), we sum the integrals calculated on each sub-tetrahedron of the polyhedron  $P_1^K$  arisen after the tetrahedralization of the latter by using the dofs defined on the entire element  $K$ ;
- in the case of two physical parts (right), we sum the integrals calculated on each sub-tetrahedron of  $P_1^K$  by using the dofs indicated by  $i', j', k'$ , and the same strategy is applied on each sub-tetrahedron of  $P_2^K$  by using the dofs indicated by  $i'', j'', k''$ .

We point out that the same procedure is applied also when considering the cut-faces for integrating the DG terms on the fluid-structure interface and on the fluid-fluid interface (i.e. on  $\Sigma$  and  $\mathcal{F}_{h,phy}^i$ , respectively, see Section 2).

This procedure is able to treat efficiently cases of high geometric complexity and in particular the case of split elements.

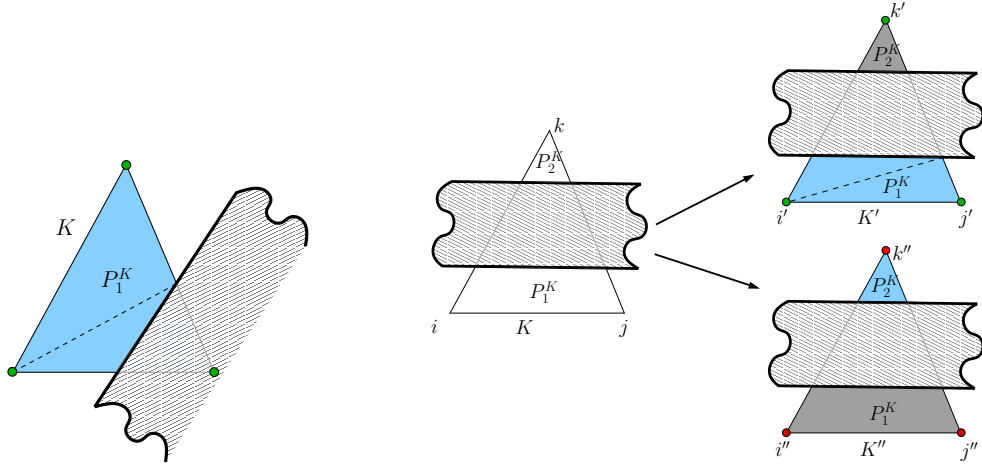


Figure 12: Computation of the integrals over the partially-overlapped elements. Left: case of one physical part (in blue) with the dofs highlighted in green. Right: case of two physical parts (in blue). The integral on each part uses a different set of dofs,  $i', j', k'$  (in green) for  $P_1^K$ ,  $i'', j'', k''$  (in red) for  $P_2^K$ .

## 4 Numerical examples

In this Section, we present some numerical results aiming at assessing the effectiveness of the proposed method. In Section 4.1, we consider a preliminary test case on a three-dimensional (3D) cube where an homogeneous elliptic problem is solved and the relative convergence of the method is verified, while in Section 4.2 we consider the same problem but with heterogeneous coefficients to prove the reliability of the proposed method with respect to the standard Finite Element Method (FEM). Then, in Section 4.3 we consider a linear steady FSI problem

given by a thick plate immersed in a fluid, while in Section 4.4 the results of a non-linear FSI problem in a time-dependent framework are reported.

The method presented in Section 2 and 3 have been implemented in the C++ finite element library LifeV ([www.lifev.org](http://www.lifev.org)).

#### 4.1 Three-dimensional Poisson problem

In this preliminary test case, we consider the Poisson equation on a simple 3D domain divided into two parts as reported in Figure 13 (left) and where we impose the continuity of the solution at the interface  $\Sigma$ . Referring to Figure 13 (left), we have the following problem

$$\begin{cases} -\Delta u = f & \text{in } \Omega^f \cup \Omega^s, \\ u = 0 & \text{on } \Gamma^f, \\ \llbracket u \rrbracket = 0 & \text{on } \Sigma, \\ \llbracket \nabla u \rrbracket \cdot \mathbf{n} = 0 & \text{on } \Sigma, \end{cases} \quad (7)$$

where  $\Omega^s = (0.25, 0.75)^3 m$ ,  $\Omega^f = (0, 1)^3 m \setminus \overline{\Omega^s}$ ,  $\Sigma \equiv \partial\Omega^s$ ,  $\Gamma^f = \partial\Omega^f \setminus \Sigma$  and  $f = 3\pi^2 \sin(\pi x) \sin(\pi y) \sin(\pi z)$ . Notice that, accordingly to the notation of Section 2, for the sake of exposition we still name the two subdomains  $\Omega^f$  and  $\Omega^s$ . We stress however that in this case there is no any fluid and structure subproblems. At the interface  $\Sigma$  between the two domains, we impose the continuity of the solution and of its normal derivative. Of course, this problem is equivalent to the monolithic one where the Poisson equation is solved in  $\Omega^f \cup \Omega^s$ . The analytic solution is

$$u(\mathbf{x}) = \sin(\pi x) \sin(\pi y) \sin(\pi z).$$

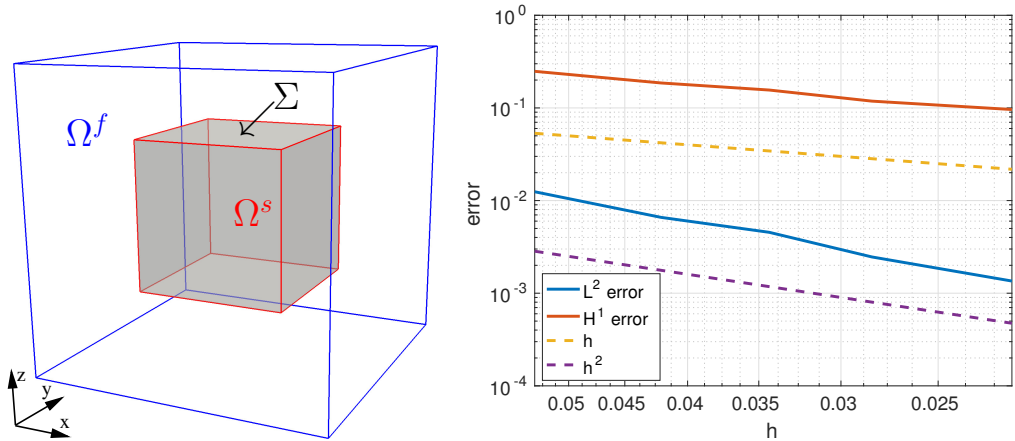


Figure 13: Left: sketch of the domains: the solid domain (red, shaded) in the middle of the full domain (blue). Right: plot of the error in  $L^2$  and  $H^1$  norm with respect to  $h$ .

	# tetrahedra in $\mathcal{T}_h^f$	# tetrahedra in $\mathcal{T}_h^s$	$h_{ave}$
1	$3.7 \cdot 10^4$	$5.1 \cdot 10^3$	0.053
2	$7.5 \cdot 10^4$	$1.0 \cdot 10^4$	0.042
3	$1.4 \cdot 10^5$	$2.1 \cdot 10^4$	0.034
4	$2.4 \cdot 10^5$	$3.9 \cdot 10^4$	0.028
5	$4.9 \cdot 10^5$	$8.9 \cdot 10^4$	0.021

Table 1: Meshes used for the convergence test.  $h_{ave}$  is the average step size of the corresponding meshes

We consider five pairs of meshes with increasing refinement and we compute the error of the numerical solution with respect to the analytic one. In Table 1, we report for each pair of meshes the number of tetrahedra of the mesh  $\mathcal{T}_h^f$  that covers the entire domain  $\Omega^f \cup \Omega^s$ , the number of tetrahedra of the mesh  $\mathcal{T}_h^s$  that covers the domain  $\Omega^s$ , and the average spatial size  $h_{ave}$ . We point out that the two meshes are completely arbitrary and non-conforming at the interface.

According to (6), the discrete formulation of the problem given by (7) reads: find  $(u_h^f, u_h^s) \in \mathbf{V}_h$  such that

$$\begin{aligned}
& \sum_{i=f,s} \int_{\Omega^i} \nabla u_h^i \nabla v_h^i - \int_{\Sigma} \{ \{ \nabla u_h \} \}_F \cdot \mathbf{n} [v_h]_F - \int_{\Sigma} [u_h]_F \{ \{ \nabla v_h \} \}_F \cdot \mathbf{n} \\
& + \frac{\gamma_{\Sigma}}{h_F} \int_{\Sigma} [u_h]_F [v_h]_F + g_h(u_h^f, v_h^f) + \sum_{i=1, \dots, N^f} \sum_{F \in \mathcal{F}_{h,phy}^i} \left\{ - \int_F \{ \{ \nabla u_h^f \} \}_F \cdot \mathbf{n} [v_h^f]_F \right\} \\
& + \sum_{i=1, \dots, N^f} \sum_{F \in \mathcal{F}_{h,phy}^i} \left\{ - \int_F [u_h^f]_F \{ \{ \nabla v_h^f \} \}_F \cdot \mathbf{n} + \frac{\gamma_{phy}^v}{h_F} \int_F [u_h^f]_F [v_h^f]_F \right\} = \\
& \sum_{i=f,s} \int_{\Omega^i} f_h^i v_h^i \quad \forall (v_h^f, v_h^s) \in \mathbf{V}_h,
\end{aligned}$$

where, referring to the notation introduced in Section 2,  $\mathbf{V}_h = \{v_h \in L^2(\bar{\Omega}^f) : v_h \in C^0(\Omega_h^0), v_h|_K \in \mathbb{P}^1, \forall K \in \mathcal{T}_h^i \text{ for } i = 0, \dots, N^f, v_h|_{\Gamma^f} = 0\} \times \{v_h \in C^0(\Omega^s) : v_h|_K \in \mathbb{P}^1, \forall K \in \mathcal{T}_h^s\}$ , with  $\mathcal{T}_h^i, i = 0, \dots, N^f$ , defined in (2.2) and (2.2),  $\gamma_{\Sigma} > 0$  and  $\gamma_{phy}^v > 0$  are penalty parameters and

$$g_h(u_h^f, v_h^f) = \gamma_g \sum_{i=1, \dots, N^f} \sum_{F \in \mathcal{F}_{h,\Sigma}^i} h_F \int_F [ \nabla u_h^f ]_F \cdot \mathbf{n} [ \nabla v_h^f ]_F \cdot \mathbf{n},$$

is the ghost penalty term with  $\gamma_g > 0$ . For the simulations, we choose  $\gamma_{\Sigma} = \gamma_{phy}^v = 10^3$  and  $\gamma_g = 1$ .

In Figure 13 (right), we report the behavior of the  $L^2$  and  $H^1$  error with respect to the mesh step size  $h$ . We see that the error is optimal for both the

norms as in the standard finite element method. In Figure 14, we plot the meshes and the solution in the case number 2 of Table 1 on a slice that cuts the entire domain at  $z = 0.5m$ . This test case shows the reliability of the proposed method to treat unfitted meshes without loss of the order of convergence when considering cut elements and non-conforming interfaces.

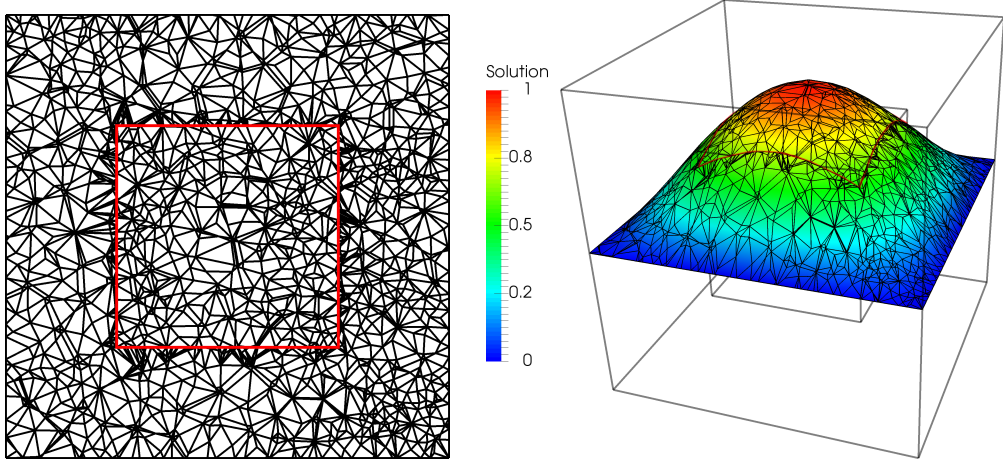


Figure 14: Left: top view of the resulting mesh on a slice ( $z = 0.5m$ ) that intersects the meshes  $\mathcal{T}_h^f$  and  $\mathcal{T}_h^s$  labelled as number 2 in Table 1. Right: the solution on the same slice. The interface is highlighted in red.

## 4.2 Poisson problem with heterogeneous coefficients

In this test case, we consider the Poisson problem with jumping diffusion parameters across  $\Sigma$  and compare our approach with the classical FEM. The problem we consider is:

$$\begin{cases} -\nabla \cdot (\eta(\mathbf{x}) \nabla u) = f & \text{in } \Omega^f \cup \Omega^s, \\ u = 0 & \text{on } \Gamma^f, \\ \llbracket u \rrbracket = 0 & \text{on } \Sigma, \\ \llbracket \eta(\mathbf{x}) \nabla u \rrbracket \cdot \mathbf{n} = 0 & \text{on } \Sigma, \end{cases}$$

where  $f = 3\pi^2 \sin(\pi x) \sin(\pi y) \sin(\pi z)$ , and  $\eta(\mathbf{x})$  is piecewise constant in each subdomain:

$$\eta(\mathbf{x}) = \begin{cases} \eta_f = \frac{1}{2} & \text{in } \Omega^f, \\ \eta_s = 3 & \text{in } \Omega^s. \end{cases}$$

At the interface  $\Sigma$  we impose the continuity of the solution and of its co-normal derivative. Again, this problem coincides with the monolithic one. In this case, the solution presents a discontinuity of its derivative along the normal direction at the interface.

To prove the effectiveness of the XFEM/DG approach with respect to the classical FEM, we consider the following frameworks:

- in the XFEM/DG approach we consider two unfitted meshes,  $\mathcal{T}_h^f$  for solving the problem on  $\Omega^f$  and  $\mathcal{T}_h^s$  on  $\Omega^s$ , so that the boundary of  $\Omega^s$  coincide with the interface  $\Sigma$ ;
- in the classical FEM approach a single mesh  $\mathcal{T}_h^{FEM}$  is used to solve the problem on the entire domain.

We use the pair of meshes number 2 of Table 1 and we choose  $\mathcal{T}_h^{FEM} \equiv \mathcal{T}_h^f$ , so that, for generality purposes, the FEM mesh is not fitting the interface  $\Sigma$ . Finally, we choose  $\gamma_\Sigma = \gamma_{phy}^v = 10^3$  and  $\gamma_g = 1$ .

In Figure 15, we plot a comparison of the solutions with the two approaches along the plane  $z = 0.5m$ . The value of the solution is reported both as the height of the plot and by means of colours. In the XFEM/DG case, it is clearly visible the discontinuity of the derivative of the solution along the interface  $\Sigma$ , while the classical FEM approach is not able to capture such a discontinuity as it is evident from the smoother solution obtained in this case.

### 4.3 Steady and linear FSI problem

In the following test case, we consider the steady-state solution of a viscous fluid that interacts with a linear elastic thick solid in the small deformations regime. In particular, we consider the Stokes equation for the fluid and the Hooke law for the solid. In this case, the velocity continuity condition at the interface  $\Sigma$  is  $\mathbf{u} = \mathbf{0}$ , and the stresses continuity condition reads  $\mathbf{T}^f \mathbf{n}^f = -\mathbf{T}^s \mathbf{n}^s$ . We obtain the following problem:

$$\left\{ \begin{array}{ll} -\nabla \cdot \left( -p\mathbf{I} + 2\mu^f D(\mathbf{u}) \right) = \mathbf{0} & \text{in } \Omega^f, \quad (8a) \\ \nabla \cdot \mathbf{u} = 0 & \text{in } \Omega^f, \quad (8b) \\ -\nabla \cdot (\lambda^s (\nabla \cdot \mathbf{d}) \mathbf{I} + 2\mu^s D(\mathbf{d})) = \mathbf{0} & \text{in } \Omega^s, \quad (8c) \\ \mathbf{u} = \mathbf{0} & \text{on } \Sigma, \quad (8d) \\ \mathbf{T}^f(\mathbf{u}, p) \mathbf{n}^f = -\mathbf{T}^s(\mathbf{d}) \mathbf{n}^s & \text{on } \Sigma, \quad (8e) \end{array} \right.$$

where  $\mu^f = 0.5Pa \cdot s$ ,  $\lambda^s = 3Pa$ ,  $\mu^s = 3Pa$ . We consider the domain  $\Omega = (0, 1)^3 m$ ,  $\Omega^s = (0.15, 0.85) m \times (0.4, 0.6) m \times (0.31, 0.34) m$  and  $\Omega^f = \Omega \setminus \overline{\Omega^s}$ , see Figure 16. Regarding the boundary conditions, we impose  $\mathbf{T}^f \mathbf{n} = (0, 0, -0.002) Pa$  on  $\Gamma_{in}$ ,  $\mathbf{T}^f \mathbf{n} = \mathbf{0}$  on  $\Gamma_{out}$  and  $\mathbf{u} = \mathbf{0}$  on the remaining fluid boundary, where  $\mathbf{n} = \mathbf{n}^f = -\mathbf{n}^s$ . On the solid we impose  $\mathbf{d} = \mathbf{0}$  at  $\Gamma_{wall}^s = \{0.15\} m \times (0.4, 0.6) m \times (0.31, 0.34) m \cup \{0.85\} m \times (0.4, 0.6) m \times (0.31, 0.34) m$ , so that it is fixed on the two sides. We impose the interface conditions (8d) and (8e) on  $\Sigma = \partial\Omega^s \setminus \Gamma_{wall}^s$ . We point out that, accordingly with the proposed

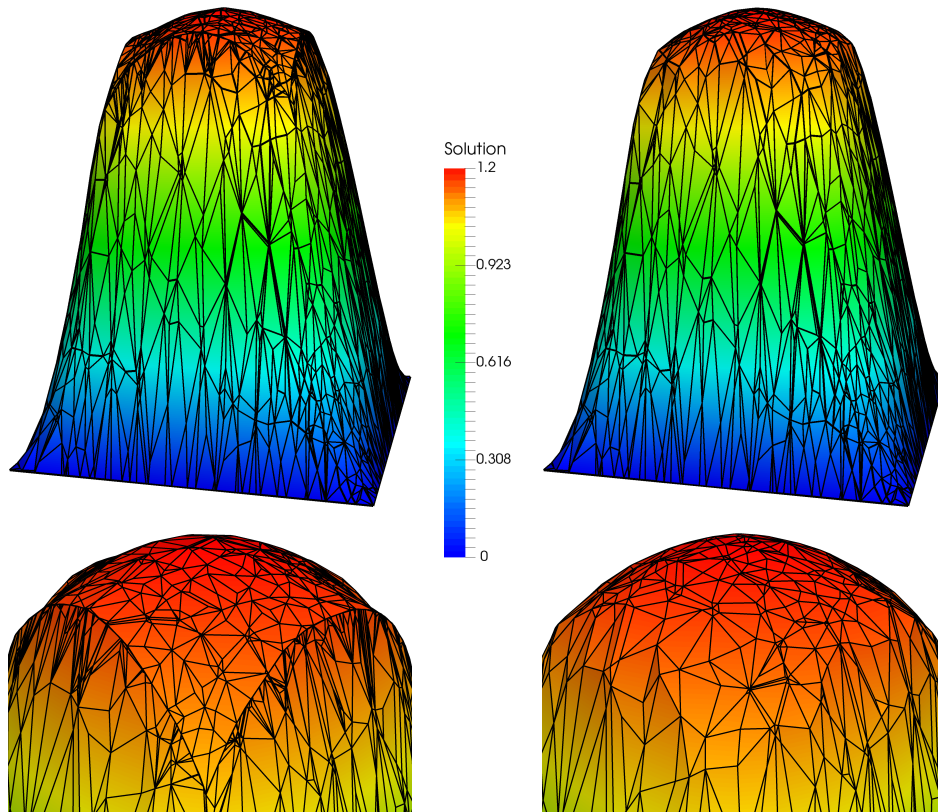


Figure 15: Plot of the numerical solution (top) and a detail (bottom) on a slice at  $z = 0.5m$  that crosses the domain with the XFEM/DG approach (left) and the classical FEM approach (right).

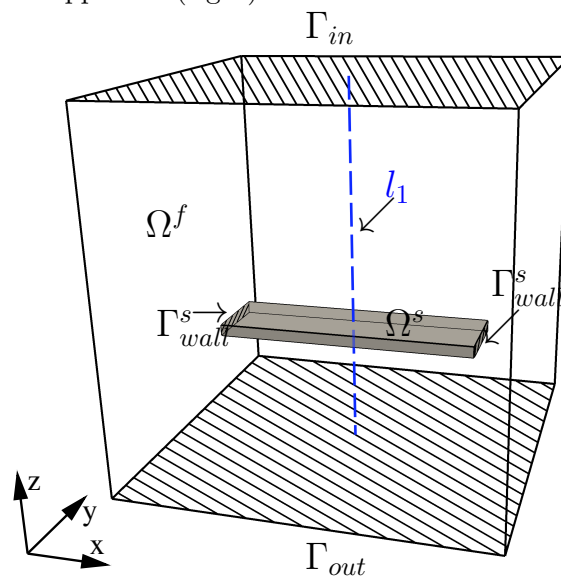


Figure 16: Sketch of the domain  $\Omega$  with the domain  $\Omega^s$  highlighted in grey.

method, the conditions on the interface  $\Sigma$  are imposed weakly by means of the DG formulation.

For the numerical simulation, we employ a fluid mesh  $\mathcal{T}_h^f$  with  $7.5 \cdot 10^4$  tetrahedra and a solid mesh  $\mathcal{T}_h^s$  composed by  $4.0 \cdot 10^4$  tetrahedra. We choose  $\gamma_\Sigma = 10^2$ ,  $\gamma_{phy}^v = 10^3$ ,  $\gamma_p = 10^{-3}$ ,  $\gamma_{com}^p = 1$  and  $\gamma_g = 10$ . The weight  $\alpha$  used for the mean operator on  $\Sigma$ , see eq. (4), is set to 0.5.

In Figure 17, we report the fluid velocity field and the structure displacement obtained by the XFEM/DG method. In Figure 18 (top), we plot the fluid pressure field on the plane  $y = 0.5m$  that cuts the structure domain into two parts. From these results, we observe the different value of pressure upstream and downstream the structure. A quantitative representation of the pressure is shown in Figure 18 (bottom-left) along the line  $l_1 : x = 0.5m, y = 0.5m, 0 < z < 1m$ , see Figure 16. We can observe the jump of the pressure field across the structure. In Figure 18 (bottom-right), we plot the velocity magnitude profile on the same line. We observe that at the interface  $\Sigma$ , the velocity condition is fulfilled.

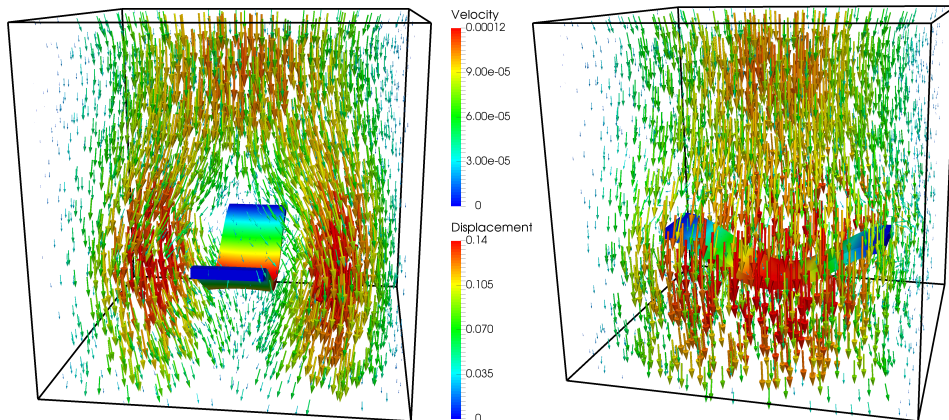


Figure 17: Plot of the velocity field (in  $m/s$ ) of the fluid and the displacement magnitude (in  $m$ ) of the structure.

Finally, in Figure 19, we show a detail of the pressure field on a slice at  $x = 0.5m$ . We see that, though some fluid elements are divided by the structure into two unconnected portions, it is possible to approximate a discontinuous solution within the same geometrical element.

#### 4.4 Time-dependent non-linear FSI problem

We consider a time-dependent FSI problem in the small deformations regime given by the coupling of the Navier-Stokes equations for the fluid and the linear

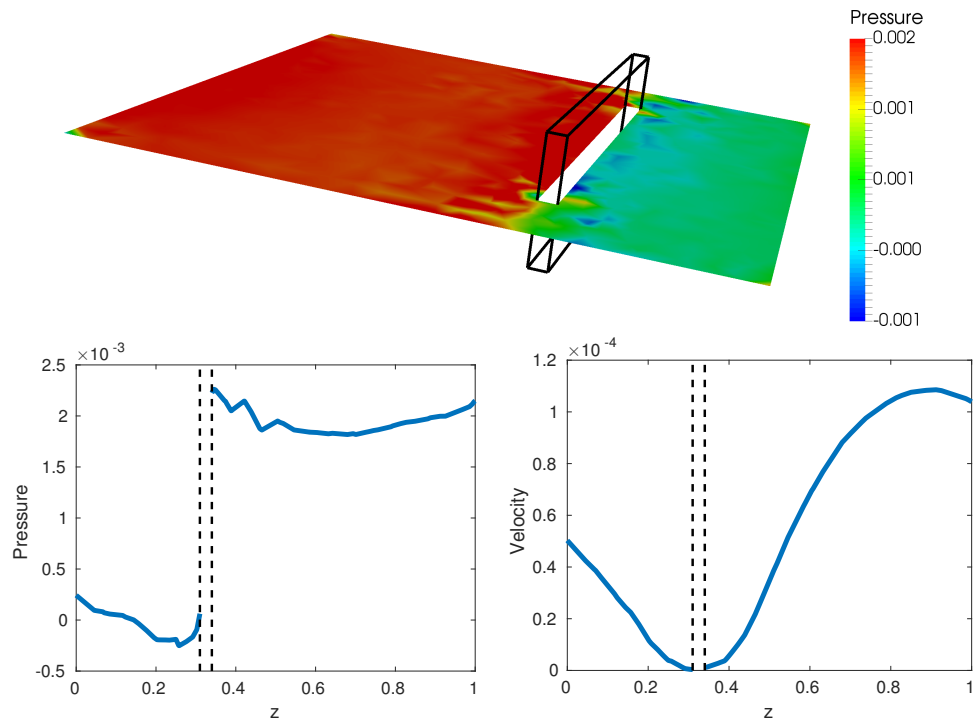


Figure 18: Top: plot of the pressure field (in  $Pa$ ) on a slice located at  $y = 0.5m$ . The outline of the structure is represented in black. Bottom: plot in the direction of the flow (line  $l_1$ ) of the pressure (left) and velocity magnitude (in  $m/s$ ) (right). The dashed lines at  $z = \{0.31, 0.34\}m$  represent the extremities of the structure.

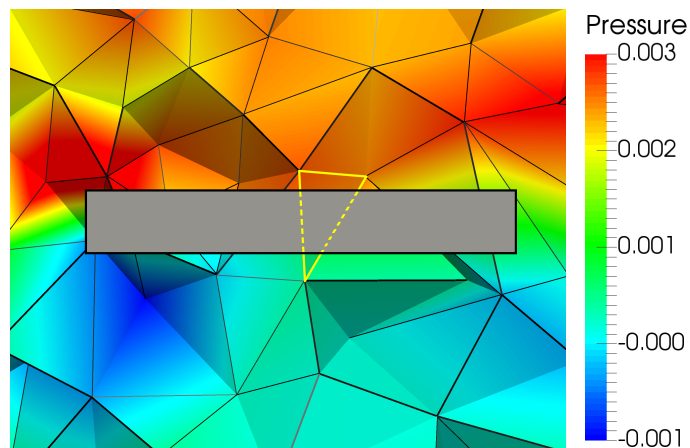


Figure 19: Detail of the pressure field (in  $Pa$ ) near the structure. It is possible to identify some tetrahedra that present a discontinuous solution within the same element, as the one highlighted in yellow.

elastic Hooke law for the structure:

$$\begin{cases} \rho^f \partial_t \mathbf{u} + \rho^f \mathbf{u} \cdot \nabla \mathbf{u} - \nabla \cdot \mathbf{T}^f(\mathbf{u}, p) = \mathbf{0} & \text{in } \Omega^f \times (0, T], \\ \nabla \cdot \mathbf{u} = 0 & \text{in } \Omega^f \times (0, T], \\ \rho^s \partial_{tt} \mathbf{d} - \nabla \cdot \mathbf{T}^s(\mathbf{d}) = \mathbf{0} & \text{in } \Omega^s \times (0, T], \\ \mathbf{u} = \dot{\mathbf{d}} & \text{on } \Sigma \times (0, T], \\ \mathbf{T}^f(\mathbf{u}, p) \mathbf{n}^f = -\mathbf{T}^s(\mathbf{d}) \mathbf{n}^s & \text{on } \Sigma \times (0, T]. \end{cases}$$

We employ the same computational domains considered in the test case reported in Section 4.3, see Figure 16, and where  $T = 48s$ . We impose a periodic sine function at the inlet, i.e.,  $\mathbf{u} = (0, 0, -0.0025 \sin(\frac{\pi}{8}t))m/s$  on  $\Gamma_{in}$ , so that we reproduce three periods,  $\mathbf{T}^f \mathbf{n} = \mathbf{0}$  on the outlet  $\Gamma_{out}$  and  $\mathbf{u} = \mathbf{0}$  on the remaining walls of the fluid boundary. As in the steady-state case, the solid is kept fixed on two of its extremities, i.e.,  $\mathbf{d} = \mathbf{0}$  at  $\Gamma_{wall}^s$ . We impose the interface conditions on  $\Sigma$ , defined in the same way as in Section 4.3. As initial conditions, we set  $\mathbf{u}(\mathbf{x}, 0) = \mathbf{0}$ ,  $\mathbf{d}(\mathbf{x}, 0) = \mathbf{0}$  and  $\dot{\mathbf{d}}(\mathbf{x}, 0) = \mathbf{0}$ . We also use the following values for the parameters:  $\rho^f = \rho^s = 1Kg/m^3$ ,  $\mu^f = 1Pa \cdot s$ ,  $\mu^s = \lambda^s = 1Pa$ .

We employ the discretization described in equation (6). For the time discretization, we use the first order BDF scheme for both the fluid and the solid and a first order linear extrapolation to treat the non-linearity of the convective term.

For the numerical simulation, we employ a fluid mesh  $\mathcal{T}_h^f$  composed by  $1.4 \cdot 10^5$  tetrahedra and a solid mesh  $\mathcal{T}_h^s$  composed by  $4.0 \cdot 10^4$  tetrahedra. The time step  $\Delta t$  is  $0.5s$ . We choose  $\gamma_\Sigma = 1$ ,  $\gamma_{phy}^v = 10^3$ ,  $\gamma_p = 10^{-2}$ ,  $\gamma_{com}^p = 10$  and  $\gamma_g = 1$ . The weight  $\alpha$  used for the mean operator on  $\Sigma$ , see eq. (4), is set to 1, so that the mortaring is taken only from the fluid side. This choice reduces the ill-conditioning of the linear system.

In Figure 20, we show the displacement of the structure at different time steps during the last cycle. In Figure 21, we plot the fluid velocity and pressure fields and the displacement magnitude of the structure at two time steps,  $t = 36s$  and  $t = 44s$ . At  $t = 36s$ , the fluid velocity goes downward the domain and reaches its maximum value. Again, the proposed method is able to capture the discontinuous nature of the pressure. In particular, we observe that the pressure is higher in the upper part of the domain. Viceversa, at  $t = 44s$ , the fluid velocity goes upward, and the pressure is higher in the lower part of the domain.

## 5 Conclusions

In this paper we have considered an unfitted Extended Finite Elements/Discontinuous Galerkin approach for the numerical solution of the fluid-structure interaction problem in the case of a thick structure. At the best of our knowledge, this is the first time that this methodology has been applied to

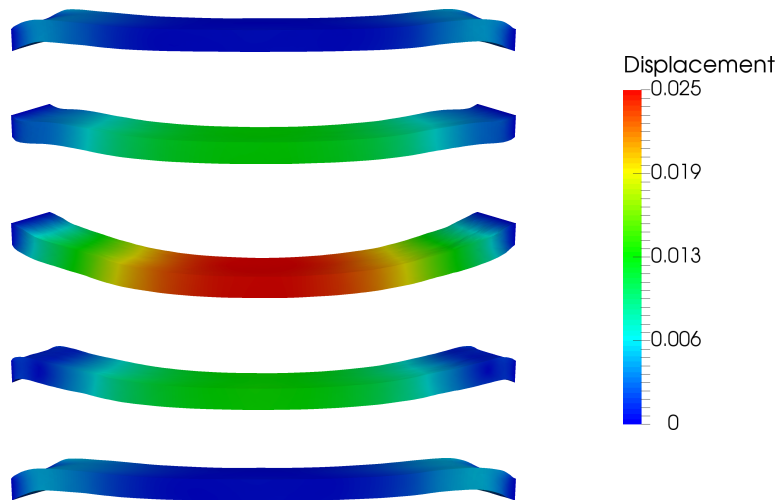


Figure 20: Post-processing of the displacement (in  $m$ ) of the structure at different time steps during the last cycle. From top to bottom:  $t = 32s$ ,  $t = 36s$ ,  $t = 40s$ ,  $t = 44s$  and  $t = 48s$ .

the case of a thick solid. To assess the effectiveness of the proposed method, we report several 3D test cases.

The main limitation of the work relies on the small displacement hypothesis. This simplifies the approach since allows one to consider a fix topology of the cut entities. The extension to the case of general displacements is undergoing and it requires the efficient handling of a variable number of dofs between time steps.

## Acknowledgments

That authors gratefully acknowledge the financial support of the Italian MIUR by the grant PRIN12, number 20121289A4XL, “Mathematical and numerical models of the cardiovascular system, and their clinical applications”.

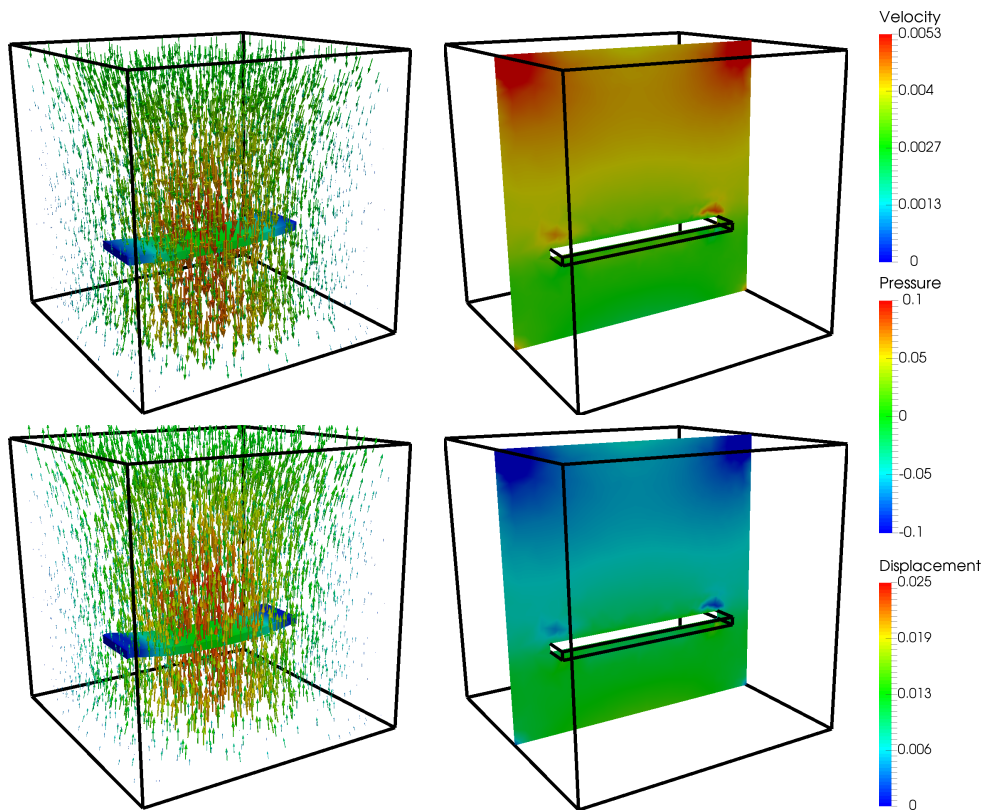


Figure 21: Numerical solution at different time steps during the last cycle:  $t = 36s$  (top),  $t = 44s$  (bottom). Left: velocity field (in  $m/s$ ) of the fluid and displacement (in  $m$ ) of the structure. Right: pressure field (in  $Pa$ ) along the plane  $y = 0.5m$ .

## References

- [1] F. Alauzet, B. Fabrèges, M. A. Fernández, and M. Landajuela. Nitsche-xfem for the coupling of an incompressible fluid with immersed thin-walled structures. *Computer Methods in Applied Mechanics and Engineering*, 301:300–335, 2016.
- [2] M. Astorino, J.-F. Gerbeau, O. Pantz, and K.-F. Traoré. Fluid-structure interaction and multi-body contact: Application to the aortic valves. *Comput. Methods Appl. Mech. Eng.*, 2009.
- [3] M. Bennoune, J. Morin-Drouin, and R. G. Owens. On the jump conditions for an immersed interface method. *SIAM Journal on Scientific Computing*, 38(3):A1280–A1316, 2016.
- [4] J. Bonet and J. Peraire. An alternating digital tree (adt) algorithm for 3D geometric searching and intersection problems. *International Journal for Numerical Methods in Engineering*, 31(1):1–17, 1991.
- [5] I. Borazjani. Fluid–structure interaction, immersed boundary-finite element method simulations of bio-prosthetic heart valves. *Computer Methods in Applied Mechanics and Engineering*, 257:103–116, 2013.
- [6] F. Brezzi and J. Pitkäranta. *On the Stabilization of Finite Element Approximations of the Stokes Equations*, pages 11–19. Vieweg+Teubner Verlag, Wiesbaden, 1984.
- [7] E. Burman. Ghost penalty. *Comptes Rendus Mathématique*, 348(21):1217–1220, 2010.
- [8] E. Burman and M. A. Fernández. An unfitted nitsche method for incompressible fluid-structure interaction using overlapping meshes. *Computer Methods in Applied Mechanics and Engineering*, 279:497–514, 2014.
- [9] L. Cattaneo, L. Formaggia, G. F. Iori, A. Scotti, and P. Zunino. Stabilized extended finite elements for the approximation of saddle point problems with unfitted interfaces. *Calcolo*, 52(2):123–152, June 2015.
- [10] S. Court and M. Fournié. A fictitious domain finite element method for simulations of fluidstructure interactions: The navierstokes equations coupled with a moving solid. *Journal of Fluids and Structures*, 55:398–408, 2015.
- [11] J. De Hart, F.P.T. Baaijens, G.W.M. Peters, and P.J.G. Schreurs. A computational fluid-structure interaction analysis of a fiber-reinforced stentless aortic valve. *Journal of Biomechanics*, 36(5):699 – 712, 2003. Cardiovascular Biomechanics.

- [12] D. A. Di Pietro and A. Ern. *Mathematical aspects of discontinuous Galerkin methods*, volume 69 of *Mathmatiques et Applications*. Springer Berlin Heidelberg, 2012.
- [13] J. Donea. An arbitrary Lagrangian-Eulerian finite element method for transient dynamic fluid-structure interaction. *Computer Methods in Applied Mechanics and Engineering*, 33:689–723, 1982.
- [14] L. Formaggia. Data structures for unstructured mesh generation. In *Handbook of Grid Generation*. CRC Press, 1998.
- [15] T.-P. Fries. Overview and comparison of different variants of the xfem. *Proceedings in applied mathematics and mechanics*, 14:27–30, 2014. GAMM 2014, Annual Meeting of the International Association of Applied Mathematics and Mechanics, 10.03.2014 - 14.03.2014.
- [16] R. Glowinski, T.-W. Pan, T. I. Hesla, and D. D. Joseph. A distributed lagrange multiplier/fictitious domain method for particulate flows. *International Journal of Multiphase Flow*, 25(5):755–794, 1999.
- [17] B. E. Griffith. Immersed boundary model of aortic heart valve dynamics with physiological driving and loading conditions. *International Journal for Numerical Methods in Biomedical Engineering*, 28(3):317–345, 2012.
- [18] S. Haeri and J. S. Shrimpton. On the application of immersed boundary, fictitious domain and body-conformal mesh methods to many particle multiphase flows. *International Journal of Multiphase Flow*, 40:38–55, April 2012.
- [19] A. Hansbo and P. Hansbo. An unfitted finite element method, based on nitsches method, for elliptic interface problems. *Computer Methods in Applied Mechanics and Engineering*, 191(47–48):5537–5552, 2002.
- [20] Y. G. Lai, K. B. Chandran, and J. Lemmon. A numerical simulation of mechanical heart valve closure fluid dynamics. *Journal of Biomechanics*, 35(7):881–892, 2002.
- [21] G. Marom. Numerical methods for fluid–structure interaction models of aortic valves. *Archives of Computational Methods in Engineering*, 22(4):595–620, 2015.
- [22] G. Marom, H.-S. Kim, M. Rosenfeld, E. Raanani, and R. Haj-Ali. Fully coupled fluid-structure interaction model of congenital bicuspid aortic valves: effect of asymmetry on hemodynamics. *Med. Biol. Engineering and Computing*, 51(8):839–848, 2013.
- [23] A. Massing, M. G. Larson, and A. Logg. Efficient implementation of finite element methods on nonmatching and overlapping meshes in three dimensions. *SIAM Journal on Scientific Computing*, 35(1):C23–C47, 2013.

- [24] R. Mittal and G. Iaccarino. Immersed boundary methods. *Annual Review of Fluid Mechanics*, 37(1):239–261, 2005.
- [25] S. E. Mousavi and N. Sukumar. Numerical integration of polynomials and discontinuous functions on irregular convex polygons and polyhedrons. *Computational Mechanics*, 47(5):535–554, 2011.
- [26] S. Natarajan, D. R. Mahapatra, and S. P. A. Bordas. Integrating strong and weak discontinuities without integration subcells and example applications in an xfem/gfem framework. *Int. J. Numer. Meth. Engng.*, 83(3):269–294, 2010.
- [27] C. S. Peskin. The immersed boundary method. *Acta Numerica*, 11:479–517, 1 2002.
- [28] B. Schott and W. A. Wall. A new face-oriented stabilized xfem approach for 2d and 3d incompressible navierstokes equations. *Computer Methods in Applied Mechanics and Engineering*, 276:233–265, 2014.
- [29] J. R. Shewchuk. Delaunay refinement algorithms for triangular mesh generation. *Computational Geometry*, 22(1):21 – 74, 2002.
- [30] H. Si. Tetgen: A quality tetrahedral mesh generator and three-dimensional delaunay triangulator. Technical report, WIAS, 2006.
- [31] F. Sturla, E. Votta, M. Stevanella, C. A. Conti, and A. Redaelli. Impact of modeling fluid-structure interaction in the computational analysis of aortic root biomechanics. *Medical Engineering & Physics*, 35(12):1721–1730, 2013.
- [32] Y. Sudhakar and W. A. Wall. Quadrature schemes for arbitrary convex/concave volumes and integration of weak form in enriched partition of unity methods. *Computer Methods in Applied Mechanics and Engineering*, 258:39–54, 2013.
- [33] R. Temam. Navier stokes equations. *Amsterdam-New York-Oxford*, 1977.
- [34] R. van Loon, P. D. Anderson, F. N. van de Vosse, and S. J. Sherwin. Comparison of various fluidstructure interaction methods for deformable bodies. *Computers & Structures*, 85(11-14):833–843, 2007. Fourth MIT Conference on Computational Fluid and Solid Mechanics.
- [35] G. Ventura and E. Benvenuti. Equivalent polynomials for quadrature in heaviside function enriched elements. *Int. J. Numer. Meth. Engng.*, 102:688–710, 2015.
- [36] E. Votta, T. B. Le, M. Stevanella, F. Fusini, E. G. Caiani, A. Redaelli, and F. Sotiropoulos. Toward patient-specific simulations of cardiac valves: State-of-the-art and future directions. *Journal of Biomechanics*, 46(2):217–228, 2013. Special Issue: Biofluid Mechanics.

- [37] E. J. Weinberg and M. R. Kaazempur Mofrad. Transient, three-dimensional, multiscale simulations of the human aortic valve. *Cardiovascular Engineering*, 7(4):140–155, 2007.

## MOX Technical Reports, last issues

Dipartimento di Matematica  
Politecnico di Milano, Via Bonardi 9 - 20133 Milano (Italy)

- 34/2016** Menafoglio, A.; Secchi, P.  
*Statistical analysis of complex and spatially dependent data: a review of Object Oriented Spatial Statistics*
- 33/2016** Antonietti, P. F.; Ferroni, A.; Mazzieri, I.; Quarteroni, A.  
*hp-version discontinuous Galerkin approximations of the elastodynamics equation*
- 32/2016** Tarabelloni, N.; Schenone, E.; Collin, A.; Ieva, F.; Paganoni, A.M.; Gerbeau, J.-F.  
*Statistical Assessment and Calibration of Numerical ECG Models*
- 30/2016** Abramowicz, K.; Häger, C.; Pini, A.; Schelin, L.; Sjöstedt de Luna, S.; Vantini, S.  
*Nonparametric inference for functional-on-scalar linear models applied to knee kinematic hop data after injury of the anterior cruciate ligament*
- 31/2016** Antonietti, P.F.; Merlet, B.; Morgan, P.; Verani, M.  
*Convergence to equilibrium for a second-order time semi-discretization of the Cahn-Hilliard equation*
- 29/2016** Miglio, E.; Parolini, N.; Penati, M.; Porcù, R.  
*GPU parallelization of brownout simulations with a non-interacting particles dynamic model*
- 28/2016** Antonietti, P.F.; Dal Santo, N.; Mazzieri, I.; Quarteroni, A.  
*A high-order discontinuous Galerkin approximation to ordinary differential equations with applications to elastodynamics*
- 26/2016** Brunetto, D.; Calderoni, F.; Piccardi, C.  
*Communities in criminal networks: A case study*
- 27/2016** Repossi, E.; Rosso, R.; Verani, M.  
*A phase-field model for liquid-gas mixtures: mathematical modelling and Discontinuous Galerkin discretization*
- 25/2016** Baroli, D.; Cova, C.M.; Perotto, S.; Sala, L.; Veneziani, A.  
*Hi-POD solution of parametrized fluid dynamics problems: preliminary results*